Turkish Journal of Electrical Engineering & Computer Sciences

http://journals.tubitak.gov.tr/elektrik/

Research Article

Turk J Elec Eng & Comp Sci
() : –
© TÜBİTAK
doi:10.3906/elk-2105-210

Scattering analyses of arbitrary roughness from 2-D perfectly conductive periodic surfaces with moments method

Yunus Emre YAMAÇ*, Ahmet KIZILAY
Department of Electronics and Communication Engineering, Yıldız Technical University, İstanbul, Turkey

Received: 21.05.2021 • **Accepted/Published Online:** 14.12.2021 • **Final Version:** ..2022

Abstract: In this paper, a periodic-MoM-based code with high accuracy performance is developed to calculate electromagnetic scattering from a periodic conductive surface in two dimensions with any degree of roughness. Firstly, the existing separate methods in the literature are reviewed step by step to compose a periodic-MoM solution for 2-D periodic surfaces. Then, the dynamic selection of optimal formulation of the periodic-MoM solutions created using these existing methods is evaluated to reduce solution time and obtain high accuracy. In this study, the performance parameters of the existing methods are investigated in solving a real 3-D scattering problem by a periodic-MoM for the first time in the literature. Eventually, a commercial EM solver with a similar numerical approach is employed for comparison, validation, and accuracy achievements of these different periodic-MoM formulations. Furthermore, an analytical solution named Floquet mode-matching method (FMMM) is developed based on the Rayleigh hypothesis for slightly rough surfaces, and the accuracy of the code is tested using this analytical solution. This study is entirely compatible with analytical solutions and gives better results than this commercial EM solver in terms of accuracy. Also, the FMMM formulation derived for comparison provides a more straightforward solution than the small perturbation method (SPM), a classical solution method, and it is adapted to two-dimensional surface roughness for the first time in this paper. However, this full-wave solution has no restriction on surface roughness, unlike the analytical solutions.

Key words: FMMM, MoM, periodic rough surfaces, PGF, SPM

1. Introduction

For optics and remote sensing applications, modeling a surface of a medium such as a sea and ground, and calculating electromagnetic scattering from these surfaces has been an essential subject for researchers from past to present. The majority of analytic and numerical solutions for this forward bi-static scattering problem have been focused on random or arbitrary rough conductive or dielectric surfaces with single- or multilayer to model artificial and natural rough surfaces [1–14]. One of the well-known classical solutions of a rough surface is the small perturbation method (SPM), initially derived by Rice in the 1950s [1]. Rice reported that the sinusoidal and random slightly rough surfaces could be solved analytically with first- and second-order SPM. This method is based on Lord Rayleigh's assumption that the scattered fields consist of the sum of up-and-down-going plane waves, and it is proved that the roughness of surfaces has restrictions in the Rayleigh hypothesis [2]. Besides, when the order of the solution increases, the scattering coefficients turn out to be highly complicated in the SPM [3]. In order to increase the convergence of the related series in the SPM theory, especially for multilayer interfaces, an iterative method should be employed to determine higher-order coefficients [4, 5]. Moreover, an

*Correspondence: yeyamac@yildiz.edu.tr

This work is licensed under a Creative Commons Attribution 4.0 International License.

alternative solution approach called Rayleigh–Fourier or Floquet mode-matching method (FMMM) based on the Rayleigh hypothesis without perturbation theory is also reported [6, 7]. In this method, the scattering from one-dimensional sinusoidal surfaces can be easily calculated with Bessel functions [6].

Integral equations (IEs), in conjunction with the method of moments (MoM) solution, are among the most commonly used methods treating rough surface scattering problems. However, there are several IE approaches to deal with these types of problems. The physical constraints are taken into account in determining the approaches, and the solution domain is bounded due to real antenna radiation. A tapered beam is exercised as the first approach to avoid edge singularity [8]. The approach's main drawbacks are increasing the solution domain and loss of accuracy at large incidence angles. Since the wavefront of the wave radiating from the antenna is assumed to turn into a plane wave, a far-reaching effect on the rough surface arises at very low grazing angles. Unwanted radiations can still occur by the edges of the solution domain that has to be physically truncated for near-grazing angle problems in the tapered beam approach. The solution domain is bounded with a cancellation method of edge effects as the second approach. For this purpose, the resistive strips can be added to boundaries to overcome this problem [9]. The rough surfaces can also be modeled as a bounded perturbation with a new formulation [10]. The scattered fields are conceded as perturbations from local roughness. The incident wave can be assumed as a plane wave rather than a tapered beam in this near grazing illumination approach. The third approach is the periodic-surface moment method [11] or named electric field integral equation-method of moments (EFIE-MoM) method in [7]. This method is an alternative solution in order to obtain the scattering from rough surfaces. Compared to artificial illumination with a tapered beam as the solution domain grows at small grazing angles, the periodic surface moment method reduces the computational burden for these types of problems and avoids singularity at the surface edges [11]. In this approach, the random surface partition is selected, and the remaining part is considered periodic [12]. Besides, there are also different approaches in the literature in order to solve IEs. A closed-form of classical PGF via using complex image technique has been obtained for arbitrary rough surfaces [13], as well as a numerical method based on the calculation of the Green's function (GF) of a locally rough interface with and without any periodicity as perturbation series of internal and external roughness is also reported for direct and inverse scattering problems [14].

An EFIE-based periodic-MoM solution is obtained after a detailed review process of available formulations in this paper. The periodic-MoM code is generated for perfectly conducting surfaces simulating a sea or wet soil, then the resulting EFIE is solved to calculate scattering from the surfaces with arbitrary roughness. The infinite surface is considered periodic to prevent edge effects, and free space-periodic Green's function (FS-PGF) is chosen to be the IE's kernel. The convergence problem of the FS-PGF is addressed by the acceleration techniques suggested in [15–22], and the acceleration techniques are compared for frequency, dimensions of the unit cell, and surface height. Additionally, the modified Rao-Wilton-Glisson (RWG) basis and testing functions can model the non-zero component of the current on the boundaries as in [23, 24]. Consequently, the methods employed in the periodic-MoM formulations consist of the discretization of the periodic surface currents by special basis and testing functions for inner and boundary edges to provide the continuity of surface current and the acceleration of the PGF's double series sum by Kummer's and Ewald's transformations. These two major acceleration techniques are compared within a MoM code in detail to handle realistic 3-D scattering problems. Besides, singularities that will arise in these methods are discussed, and the extraction of near- and far-field equations is also given in this study.

Moreover, the verification and accuracy of the EFIE-MoM solution are benchmarked with Rayleigh-based

solutions and commercial software. For this purpose, a commercial software package (FEKO) is employed for comparison, validation, and accuracy achievements. The MoM solution is analytically compared to Rayleigh-based methods for slightly rough 2-D surfaces. Therefore, the proposed full-wave solution agrees well with Rayleigh-based methods and yields higher accuracy than FEKO. Besides, the EFIE-MoM has no restrictions on the surface's roughness, and even highly rough surfaces can be solved by this method, unlike the analytical solutions. Also, the formulation of the FMMM that can produce a more comfortable solution than SPM is obtained and utilized for comparison. In the paper's organization, the formulations of the EFIE-MoM solution are given in detail in Section 2. The validations and performance tests of the periodic-MoM formulations for several cases are carried out with FMMM, conventional arbitrary-order SPM, and FEKO software in Section 3. Furthermore, a helpful general semianalytical and a specific analytical solution of the FMMM for arbitrary and sinusoidal periodic surfaces are also derived and given in Appendices 1 and 2, respectively. Here, these 2-D FMMM formulations are derived for the first time in this paper.

2. Formulation

Assume that a plane wave is an incident on a periodic conductive rough surface $\{z = f(x,y)\}$ with the incidence angles of θ_i and ϕ_i as represented in Figure 1. As shown in Figure 1, the PEC surface is located on the x–y plane, and the upper region of this surface is the vacuum. $\overline{a}_1$ and $\overline{a}_2$ are the primitive lattice vectors, and L_x and L_y are the dimensions of the unit cell. The rough surface is periodic with L_x and L_y, and the surface function satisfies the condition of the periodicity $\{z = f(x,y) = f(x+L_x, y+L_y)\}$. The polarization of the incident plane wave can be determined according to the transverse to the z-direction of electric and magnetic fields. Therefore, under the assumption of $e^{j\omega t}$ time dependence, the incident electric field is expressed as follows

$$\overline{E}_i = \hat{e}_i E_0 e^{-j\overline{k}_i\cdot\overline{r}} = (\hat{\theta}\cos\alpha + \hat{\phi}\sin\alpha)E_0 e^{-j\beta_0\hat{k}_i\cdot\overline{r}} = (\hat{v}_i + \hat{h}_i)E_0 e^{-j\beta_0\hat{k}_i\cdot\overline{r}} \tag{1}$$

where α is the polarization angle and $\overline{k}_i = \beta_0\hat{k}_i$ is the incident vector of the wave. $\alpha = 0^\circ$ is θ-polarization (vertical $\hat{v}_i$ or TM polarization), and $\alpha = 90^\circ$ is ϕ-polarization (horizontal $\hat{h}_i$ or TE polarization). In (1), the incident wave vector is $\overline{k}_i = \beta_x\hat{x} + \beta_y\hat{y} - q\hat{z}$, and the wave number is $k = \beta_0 = \omega\sqrt{\mu_0\epsilon_0}$, where $\beta_x = \beta_0\sin\theta_i\cos\phi_i$, $\beta_y = \beta_0\sin\theta_i\sin\phi_i$, and $q = \beta_0\cos\theta_i$.

The general expression of the scattered field from a periodic surface seen in Figure 1 by combining with Floquet's theorem can be written as

$$\overline{E}_s(x,y,z) = \hat{e}_s \sum_{m=-\infty}^{\infty}\sum_{n=-\infty}^{\infty} e^{-j\beta_m x}e^{-j\beta_n y} f_{mn}(z) \tag{2}$$

Under the assumption of the Rayleigh hypothesis and subjecting the fields in (1) and (2) to the homogeneous Helmholtz equation, $f_{mn}(z)$ and its coefficients for each Floquet mode can be found as in Appendix 1. However, the Rayleigh assumption, as mentioned in earlier studies, will not be valid on the boundary of the surface as the result of the singularity [25]. Hence, the surface gradient should be smaller than 0.448, and the assumption is only valid for a slightly rough shallow surface [2]. It should be noted that the field expression given (2) is not a regular function in all domains, i.e. it cannot differentiate in a classical sense on the boundary. Using boundary condition on the periodic PEC surface in Figure 1, the IE of the scattered electric field $\overline{E}_s(\overline{J}_{S_p})$

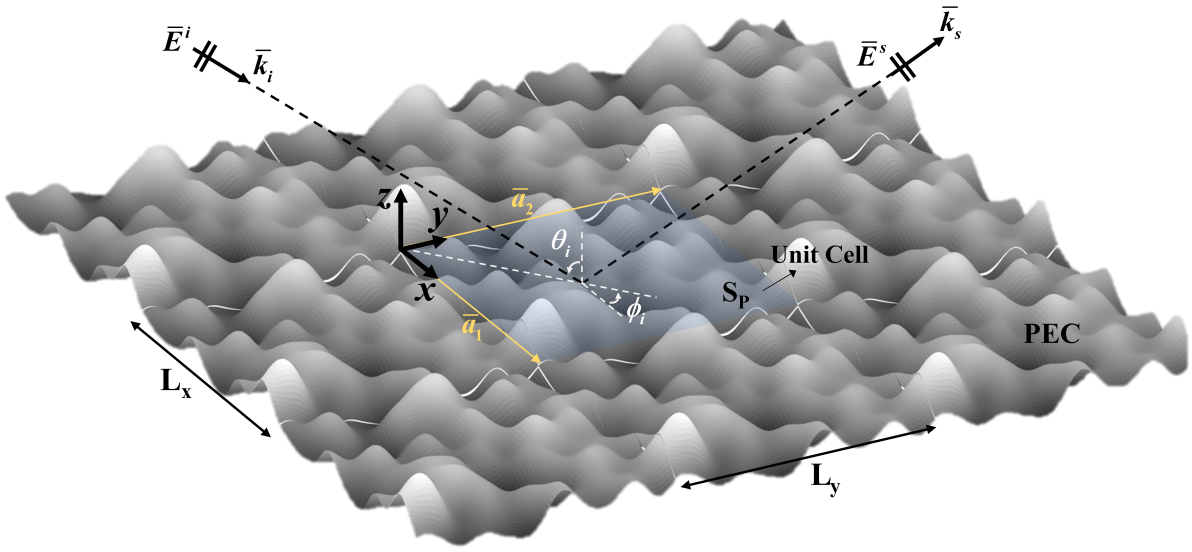


Figure 1. Configuration of a scattering problem from a unit cell of conducting periodic surfaces.

can be written in dyadic representation

$$\overline{E}^s\left(\overline{J}_{S_p}\right) = -j\omega\mu_0 \int_{S'_p} \left[\overline{\overline{I}} + \frac{1}{\beta_0^2}\nabla\nabla\right] \cdot G_p\left(\overline{r}|\overline{r}'\right) \overline{J}_{S_p}\left(\overline{r}'\right) dS'_p \tag{3}$$

Here, $\overline{J}_{S_p}$ denotes periodic current density on the periodic surface, G_p is doubly periodic free-space Green's function, and S'_p implies the unit cell's surface domain. $\overline{\overline{I}} = \hat{x}\hat{x} + \hat{y}\hat{y} + \hat{z}\hat{z}$ is the unit dyad. The surface currents on the other unit cell may be written in terms of the current on the center unit cell as follows:

$$\overline{J}_{S_p}\left(x' + mL_x, y' + nL_y, z'\right) = e^{-j\beta_x L_x} e^{-j\beta_y L_y} \overline{J}_{S_p}\left(x', y', z'\right) \tag{4}$$

According to (4), the currents outside the center unit cell can be found by adding a phase difference to the current in a unit cell, and the added phase is in proportion to the size of the lattice, the number m and n represent the (m,n)-th cell. Using this current source approach combined with Floquet's theorem, the PGF is derived from periodically spreading point charges in the x-y plane in a lattice. However, the PGF can alternatively be obtained from free-space Green's function (spatial form) [19];

$$G_p^{spatial}\left(\overline{r}|\overline{r}'\right) = \frac{1}{4\pi} \sum_{m=-\infty}^{\infty} \sum_{n=-\infty}^{\infty} e^{-j\beta_x m L_x} e^{-j\beta_y n L_y} \frac{e^{-j\beta_0 R_{mn}}}{R_{mn}} \tag{5}$$

and Poisson's transform is applied to find the spectral form of (5) reported as [18];

$$G_p^{spectral}\left(\overline{r}|\overline{r}'\right) = -\frac{j}{2L_x L_y} \sum_{m=-\infty}^{\infty} \sum_{n=-\infty}^{\infty} \frac{e^{-j\beta_m\left(x-x'\right)} e^{-j\beta_n\left(y-y'\right)} e^{-jq_{mn}\left|z-z'\right|}}{q_{mn}} \tag{6}$$

where $\beta_m = \beta_x + 2m\pi/L_x$, $\beta_n = \beta_y + 2n\pi/L_y$, and $R_{mn} = \left\|\overline{r} - \overline{r}'_{mn}\right\|$. Here $\overline{r}$ is the observation point, $\overline{r}'_{mn}$

is the source point in the (m,n)-th cell, and

$$q_{mn} = \begin{cases} \sqrt{\beta_0^2 + \|\beta_{mn}\|^2}, & \beta_0 \geq \|\beta_{mn}\|^2 \\ -j\sqrt{\|\beta_{mn}\|^2 - \beta_0^2}, & \beta_0 < \|\beta_{mn}\|^2 \end{cases} \tag{7}$$

where $\beta_{mn} = \beta_m \hat{x} + \beta_n \hat{y}$. Also, the scattering wave propagation vector $\overline{k}_s = \overline{k}_{mn} = \hat{x}\beta_m + \hat{y}\beta_n + \hat{z}q_{mn}$, which is depicted in Figure 1, can be written by using Floquet's theorem. The total field consists of the reflected field (coherent field) as a specular reflection on a smooth surface in case of $m = n = 0$, and the scattered field as an incoherent field from the surface roughness of any other m and n. The coherent field will decrease due to the roughness leading to the scattered field's distribution in all directions.

2.1. MoM implementation

In combination with the MoM, the IE method is a rigorous and effective treatment for scattering problems from rough surfaces. By using (1) and (3) with the boundary condition, the resulting EFIE can be converted into a linear system of the equation after employing the MoM as $\overline{\overline{Z}}_{(\xi\psi)}\overline{I}_{(\psi)} = \overline{V}_{(\xi)}$. Here,

$$Z_{(\xi\psi)} = j\beta_0\eta_0\left[\int_{T_\xi^\pm}\int_{T_\psi^\pm}\left(\overline{f}_\xi(\overline{r})\cdot\overline{f}_\psi(\overline{r}')\,G_p(\overline{r}|\overline{r}') - \frac{1}{\beta_0^2}\left[\nabla_s'\cdot\overline{f}_\xi(\overline{r})\right]\left[\nabla_s'\cdot\overline{f}_\psi(\overline{r}')\right]G_p(\overline{r}|\overline{r}')\right)dS_{T_\psi^\pm}dS_{T_\xi^\pm}\right] \tag{8}$$

and

$$V_{(\xi)} = \int_{T_\xi^\pm}\overline{f}_\xi(\overline{r})\cdot\overline{E}^i dS_{T_\xi^\pm} \tag{9}$$

$\overline{f}_\xi(\overline{r})$ and $\overline{f}_\psi(\overline{r}')$ are testing and basis functions, respectively. The induced current density $\overline{J}_{S_p} = \sum_{\psi=1}^{N} I_\psi \overline{f}_\psi(\overline{r}')$ has expanded a set of basis functions, and triangular elements are used to discretize the PEC surface. A special basis and testing functions are utilized to ensure continuity of the current between unit cells' boundaries, as suggested in [24]. Three different types of basis and testing functions are needed to calculate the surface current accurately. For inner edges, well-known RWG basis functions are used [26]. Also, RWG basis and testing functions are modified to be added phase shifts with the lattice's lengths for each boundary edge. The top view of the sample basis functions is given in Figure 2 to determine proper edges and triangular element pairs for boundaries and inner edges. The first type of basis and testing functions are based on a conventional RWG basis for the inner edges. The testing function is equal to the basis function for these inner edges. The second type basis and testing functions are defined for the vertical boundary edges, and similarly, the third type basis and testing functions are defined for the horizontal boundary edges. Thus, both testing and basis functions for second and third types are given by common formulas as follows:

$$\overline{f}_\psi^{(2,3)}(\overline{r}') = \begin{cases} \overline{\rho}_\psi^+(\overline{r}')\frac{l_\psi}{2A_\psi^+}e^{-j\overline{k}_i\cdot\overline{a}_{(1,2)}}, & \overline{r}' \in T_\psi^+ \\ \overline{\rho}_\psi^-(\overline{r}')\frac{l_\psi}{2A_\psi^-}, & \overline{r}' \in T_\psi^- \\ 0, & \text{otherwise.} \end{cases}, \quad \overline{f}_\xi^{(2,3)}(\overline{r}) = \begin{cases} \overline{\rho}_\xi^+(\overline{r})\frac{l_\xi}{2A_\xi^+}e^{j\overline{k}_i\cdot\overline{a}_{(1,2)}}, & \overline{r} \in T_\xi^+ \\ \overline{\rho}_\xi^-(\overline{r})\frac{l_\xi}{2A_\xi^-}, & \overline{r} \in T_\xi^- \\ 0, & \text{otherwise.} \end{cases} \tag{10}$$

where $\overline{a}_{(1,2)}$ are the lattice's translation vectors for the second and third type basis and testing functions, respectively. The basis and testing functions are defined separately on the plus and minus triangles of the

shared edge. Thus, l_ψ is the length of the ψ-th edge and $\overline{\rho}_\psi^+ = \overline{v}_\psi^+ - \overline{r}'$, $\overline{\rho}_\psi^- = \overline{r}' - \overline{v}_\psi^-$. T_ψ^+ and T_ψ^- are the triangles of this common edge. $\overline{v}_\psi^\pm$ are the vectors that indicate free-vertices of the triangles. These expressions can be written similarly for the testing function. By substituting the findings above in (8), the resulting integrals can be solved by numerical quadrature [27]. The unknown current constants are found for each edge. The edges on boundaries are also periodic; hence, it is sufficient to find related unknowns only side of boundaries. However, the derivation of (8) will not give in this article so that it has been discussed in detail in [24].

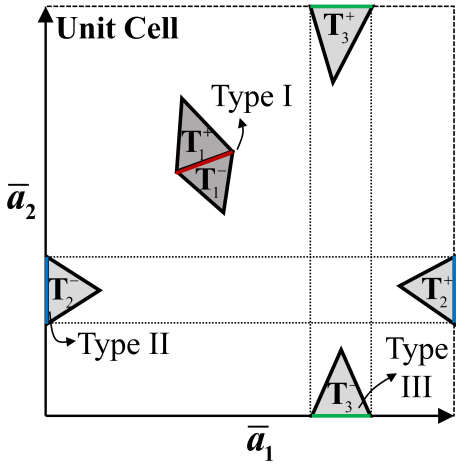


Figure 2. Top view of a unit cell for three different edge samples.

2.2. Scattering near- and far-field equations

After finding the surface current density on the periodic conductive surface, the scattered field in a near- or far-field region may be needed to evaluate it concerning the position of the observation point. Consequently, for upper half-space, i.e. $(z > (f)_{max})$; thus, $|z - z'| \to (z - z')$ and the scattering E-field:

$$\overline{E}^s\left(\overline{J}_{S_p}\right) = -j\beta_0\eta_0 \sum_{\psi=1}^{N} I_\psi \left[\int_{T_\psi^\pm} \overline{f}_\psi\left(\overline{r}'\right) G_p\left(\overline{r}|\overline{r}'\right) dS_{T_\psi^\pm} + \frac{1}{\beta_0^2} \int_{T_\psi^\pm} \overline{f}_\psi\left(\overline{r}'\right) \cdot \nabla\nabla G_p\left(\overline{r}|\overline{r}'\right) dS_{T_\psi^\pm} \right] \tag{11}$$

In order to calculate near-fields, the double gradient of the PGF shall be derived. If the spectral form of the PGF is employed

$$\nabla\nabla G_p^{spectral}\left(\overline{r}|\overline{r}'\right) = -G_p^{spectral}\left(\overline{r}|\overline{r}'\right) \overline{k}_{mn}\overline{k}_{mn} = -G_p^{spectral}\left(\overline{r}|\overline{r}'\right) \overline{k}_{mn} \otimes \overline{k}_{mn} \tag{12}$$

where $\otimes$ sign denotes tensor product. Although the spectral form PGF allows eliminating the complexity of the solution, the slowing convergence will begin a small problem at points very close to the surface. However, the convergence will not be a constraint in the far-field region (see Appendix 3 for near-field expression for observation points just above the surface $(z \leq (f)_{max})$.

2.3. Acceleration techniques

The periodicity is embedded in the kernel of the EFIE in (3) with a linear progressive phase shift as a result of Floquet's theorem. The rough surface is modeled by dividing with periodic lattices, thereby reducing the

infinite surface to a single unit cell. However, the solution of the EFIE suffers from the numerical computation of the FS-PGF due to the relevant series converging very slowly. It is vital to accelerate the doubly periodic series in obtaining numerical calculations effectively. The convergence problem arises when the surface height is low so that the observation point will be somewhat close to the surface, especially for the spectral form of PGF. The spectral PGF will converge rapidly as the observation point moves away from the surface since the spectral representation is the Fourier transform of its spatial form. In order to speed up the convergence, some decomposition techniques are fortunately reported at several studies for 1-D and 2-D periodicity of the surface [15–22].

2.3.1. Kummer's decomposition

The PGF with Kummer's transformation [19] is given as

$$G_p\left(\overline{r}|\overline{r}'\right) = G_p^{spectral}\left(\overline{r}|\overline{r}'\right) - G_p^{spectral,asymptotic}\left(\overline{r}|\overline{r}'\right) + G_p^{spatial,asymptotic}\left(\overline{r}|\overline{r}'\right) \tag{13}$$

$$G_p\left(\overline{r}|\overline{r}'\right) = \sum_{m,n=-\infty}^{+\infty} \frac{e^{-j\beta_m(x-x')}e^{-j\beta_n(y-y')}}{2L_xL_y}\left[\frac{e^{-jq_{mn}|z-z'|}}{jq_{mn}} - \frac{e^{-u_{mn}|z-z'|}}{u_{mn}}\right] + e^{-j\beta_x mL_x}e^{-j\beta_y mL_y}\frac{e^{-uR_{mn}}}{4\pi R_{mn}} \tag{14}$$

where u is the smoothing parameter, and $u_{mn} = \sqrt{\|\beta_{mn}\|^2 + u^2}$. The choice of the smoothing parameter u affects the convergence of spatial and spectral sums, so a reasonable choice of u is recommended as half size of the maximum reciprocal lattice vector [19]. For an orthogonal 2-D lattice seen in Figure 1, these vectors are $\overline{k}_1 = (2\pi/L_x)\hat{x}$ and $\overline{k}_2 = (2\pi/L_y)\hat{y}$. Thus, the smoothing parameter is $u = \pi/\min\left(L_x, L_y\right)$.

2.3.2. Ewald's method

One of the most effective ways to speed up the FS-PGF computation is Ewald's method. The PGF is decomposed into spatial and spectral forms as $G_p\left(\overline{r}|\overline{r}'\right) = G_1^{spectral}\left(\overline{r}|\overline{r}'\right) + G_2^{spatial}\left(\overline{r}|\overline{r}'\right)$ again. These decomposed functions are obtained as given in [21]:

$$G_1^{spectral}\left(\overline{r}|\overline{r}'\right) = \frac{1}{4L_xL_y}\sum_{m,n=-\infty}^{\infty}\frac{e^{-j\beta_m(x-x')}e^{-j\beta_n(y-y')}}{jq_{mn}} \times \sum_{\pm} e^{\pm j(z-z')q_{mn}}\mathrm{erfc}\left(\frac{jq_{mn}}{2E} \pm (z-z')E\right) \tag{15}$$

$$G_2^{spatial}\left(\overline{r}|\overline{r}'\right) = \frac{1}{8\pi}\sum_{m,n=-\infty}^{\infty}\frac{e^{-j\beta_x L_x}e^{-j\beta_y L_y}}{R_{mn}} \times \sum_{\pm} e^{\pm j\beta_0 R_{mn}}\mathrm{erfc}\left(R_{mn}E \pm j\frac{\beta_0}{2E}\right) \tag{16}$$

In (15) and (16), $\sum_{\pm}$ denotes the sum of the related terms with + and – signs. The derivation of the equations above will not be given in detail in this paper. In addition, the choice of the optimal value of E is essential to minimize the number of terms required to reach the desired error value for convergence. Therefore, the optimum value of E has been discussed in [21], but, in this paper, the optimum E parameter is chosen as follows:

$$E_{opt} = \pi/\sqrt{2L_xL_y} \tag{17}$$

This choice results in better convergence time over a more comprehensive frequency range. For high frequencies or large periodic spacings, a complete condition on E must be determined to avoid loss of accuracy as [20],

where $E = \max(E_{opt}, \beta_0/2H)$ and H is the maximum number to be permitted $\exp(H^2)$ in order to avoid cancellation errors.

2.4. Extractions of singular terms

In the MoM matrix calculation in (8), the self-terms should be appropriately handled to overcome 1/R singularities of the spatial GFs in accelerating the evaluations of IEs. The cancellation of potential GFs' singularity is conventionally treated by singularity subtraction and regularization approaches [28–31]. In this paper, the singularity subtraction approach is employed as follows

$$\int_{S'} \overline{f}(\overline{r}') G_p(\overline{r}|\overline{r}')\, dS' = \underbrace{\int_{S'} \overline{f}(\overline{r}') \left[G_p(\overline{r}|\overline{r}') - G_p^{asymptotic}(\overline{r} \to \overline{r}'|\overline{r}')\right] dS'}_{\text{Integrated Numerically}} + \underbrace{\int_{S'} \overline{f}(\overline{r}') G_p^{asymptotic}(\overline{r} \to \overline{r}'|\overline{r}')\, dS'}_{\text{Integrated Analytically}} \tag{18}$$

where $\overline{f}(\overline{r})$ represents the basis function. After applying this subtraction for the central cell ($m = n = 0$), the first term of the right-hand side of (18) becomes regular. The second term of the equation is singular and analytically evaluated for linear basis functions. It should be noted that all other terms except the central cell have a finite value, and numerical quadrature methods can directly evaluate the regular terms. If (18) is applied to Kummer's transform in the central cell, the decomposition for the spatial term can be written as

$$G_{Kummer}^{spatial(0,0)} = \frac{1}{4\pi}\left[\frac{e^{-uR}-1}{R}\right] + \frac{1}{4\pi R} \tag{19}$$

Furthermore, the spatial term of Ewald's transformation is found similarly

$$G_{Ewald}^{spatial(0,0)} = \frac{1}{8\pi}\left[\sum_{\pm} \frac{e^{\pm j\beta_0 R}}{R}\mathrm{erfc}(RE \pm j\beta_0/2E) - \frac{2}{R}\right] + \frac{1}{4\pi R} \tag{20}$$

Here, the first terms are integrated numerically, or the limit values of them are obtained for electrically very small triangles reported as [32]—the second term of Eqs. (19) and (20) are integrated analytically [31]. Although a more general approach based on purely numerical quadrature schemes is reported in [33, 34], the singularity subtraction method has given above still works well for this paper's problems.

3. Numerical results and discussions

Many researchers have only focused on the acceleration techniques to speed up the convergence. We will discuss whether fast convergence is the main factor in determining the performance of the numerical code in a complete MoM solution for realistic scattering problems. In combination with two major acceleration techniques, the height of the surface, mesh sizes, unit cell dimension and frequency, and quality of the numerical integration are discussed in detail to assess the performance of periodic-MoM formulations. For this purpose, the MoM formulations are compared for periodic flat, 1-D and 2-D sinusoidal, and arbitrary rough surfaces in this section. Herein, the performance analyses of numerical techniques in previous sections are performed, and the most appropriate solution approach for different scattering cases is explored.

However, before numerical calculations are carried out, it can be useful to mention the cutoff phenomena for scattering fields from an infinite periodic structure. Condition to propagate Floquet modes is $\|\beta_{mn}\| < k$, otherwise evanescent waves will occur ($\|\beta_{mn}\| > k$). Hence, cutoff frequencies for each Floquet mode can be estimated as given in (22), and this formula will be employed in finding analytical values for scattering fields from various periodic surface samples. Besides, all numerical calculations are conducted by Ryzen 3900x processor and MATLAB software in this paper.

3.1. Performance analyses of periodic-MoM formulations

In this subsection, the performance analyses of the periodic-MoM formulations alluded to in the previous sections start with a flat surface case since a flat surface can be considered a periodic surface. Also, one can easily find the analytical solution to this problem, and the flat surfaces in the z-axis complicate the achievement of acceleration techniques. For these reasons, Table 1 is first prepared for the numerical approaches' performance test in the periodic-MoM formulations. For this purpose, dimensions and types of surfaces, singularity extraction, and acceleration technique are changed, and relative errors of solutions and solution times are evaluated. Here, the definition of the relative error is given in (21). In the numerical simulations used in the preparation of Table 1, the incident angle of the plane wave is selected as $\theta^i = 60^\circ$ and $\phi^i = 0^\circ$, the polarization is horizontal, and the flat surface is discretized by triangles with an edge length of about 0.1 λ. The results are analytically compared in the far-field region ($\overline{r} = \hat{z}101$ m) for the total scattered E-field that is the sum of all Floquet modes. Also, henceforth, the amplitude of the incident plane wave is determined as a unit in all simulations, i.e. $E_0 = 1$ V/m.

A commercial software having a similar periodic-MoM approach with linear basis functions is also employed for a better comparison of the periodic-MoM formulations [35]. For this purpose, FEKO software was used for comparison for various scattering cases in Table 1. Thus, as seen from Table 1, the solution time is worse than FEKO while the accuracy of our formulations is much better. However, this shortcoming can be remedied as to be discussed in the following sections. In this paper, the exact value of PGF was calculated for each point in the triangle facets. Also, the quality of the numerical quadrature used in this paper is very high to achieve desired accuracy levels in comparison with analytical solutions. This high-quality numerical integration increases numerical quadrature points and improves the overall computation time in calculating the PGF values for all source and observation triangles. Besides, precalculated PGF values for several sample points can even be utilized to create a look-up table [22], and an interpolation algorithm estimates any other points outside these sample points. The accuracy and solution speed will depend on the efficiency and ability of this interpolation algorithm. FEKO may use a look-table and an interpolation algorithm to reduce the solution time. Since our interpolation algorithm is not fast and efficient enough for large matrices, this technique is not added to the table.

Moreover, one can easily see it from Table 1, the solution's accuracy does not change significantly with the choice of the acceleration technique. Regardless of the acceleration technique, the convergence error of the PGF may have little effect on the accuracy of the solution. On the other hand, the solution time is highly dependent on the chosen acceleration technique, frequency, size of the unit cell, and the total number of unknowns. As can be seen from Table 1, Kummer's transform can yield faster results at lower frequencies. Still, it should be noted that Ewald's transform becomes faster than Kummer's decomposition for large unit cell sizes. Similarly, if the convergence error of PGF is reduced than 10^{-3}, Kummer's transform gives prolonged results compared to Ewald's decomposition.

Table 1. Comparison of periodic MoM-formulations on flat surfaces.

Frequency (MHz)	L_x (λ)	L_y (λ)	This work					FEKO	
			Singular integration	PGF error	Acceleration technique	Relative error	Solution time (s)	Relative error	Solution time (s)
3	0.1	0.1	Khayat [33]	10^{-3}	Ewald	8.22×10^{-7}	3.50	5.31×10^{-4}	0.012
					Kummer	7.33×10^{-7}	2.00		
300					Ewald	8.16×10^{-7}	3.60	8.8×10^{-3}	0.176
					Kummer	7.27×10^{-7}	2.38		
300,000					Ewald	8.16×10^{-7}	3.51	8.8×10^{-3}	0.175
					Kummer	7.27×10^{-7}	1.95		
300	0.5	0.5		10^{-1}	Ewald	8.21×10^{-7}	262	9.9×10^{-3}	0.443
				10^{-3}		8.20×10^{-7}	328		
				10^{-4}		8.21×10^{-7}	348		
				10^{-1}	Kummer	1.30×10^{-4}	124		
				10^{-3}		7.38×10^{-7}	277		
				10^{-4}		8.23×10^{-7}	908		
			Singularity Subtraction	10^{-1}	Ewald	8.62×10^{-7}	257		
				10^{-3}		8.61×10^{-7}	319		
				10^{-4}		8.62×10^{-7}	343		
1500	1.5	1.5	Khayat [33]	10^{-3}	Ewald	1.29×10^{-5}	3085	8.9×10^{-3}	5.636
					Kummer	5.82×10^{-6}	3271		
3000					Ewald	1.48×10^{-5}	2811	8.7×10^{-3}	5.646
					Kummer	7.52×10^{-6}	2809		
30,000					Ewald	3.90×10^{-5}	899	8.8×10^{-3}	5.646
					Kummer	3.86×10^{-5}	997		

$$\text{Relative Error} = \frac{\left|\left\|\overline{E}^{s}_{analytical}(\overline{r})\right\| - \left\|\overline{E}^{s}_{numerical}(\overline{r})\right\|\right|}{\left\|\overline{E}^{s}_{analytical}(\overline{r})\right\|} \tag{21}$$

3.1.1. Effect of mesh size and cutoff phenomena for periodic surfaces

Comparing the effect of mesh size is also performed in Table 2 to assess the solution's accuracy. The incident angle is staying the same as the previous calculations. A sinusoidal surface whose function is $f(x) = -h\cos(2\pi x/L_x)$ is employed, where $h = 0.1$ m and $L_x = L_y = 0.5$ m. The solution frequency is determined as 300 MHz to stay outside the cutoff frequency range as reported in [7]. Thus, the cutoff frequencies will be emerged for each Floquet modes, and if $\|\beta_{mn}\| = k$, the minimum cutoff frequency can be obtained. If this equation is rearranged in order to obtain the minimum cutoff frequency (f_c) as follows

$$\left|\sin^2\theta_i + 2\sin\theta_i\left[\frac{mc}{f_c L_x}\cos\phi_i + \frac{nc}{f_c L_y}\sin\phi_i\right] + \left(\frac{mc}{f_c L_x}\right)^2 + \left(\frac{nc}{f_c L_y}\right)^2\right| = 1 \tag{22}$$

where c is the velocity of light in free space. For $\theta^i = 60°$, $\phi^i = 0°$, $L_x = L_y = 0.5$ m and $m = -1$, $n = 0$, the cutoff frequency (f_c) is found as 321.5 MHz from (22). Thus, the scattered E-field aroused from this sinusoidal surface will behave like a flat surface for 300 MHz. It should be noted that the cutoff frequency is dependent on the incident angles and the dimensions of the unit cell, not the surface height. As seen from Table 2, the solution's accuracy increases depending on the mesh size. Here, PGF's convergence error is constant, and the acceleration technique is Kummer's transform while Khayat's formulation is used for singularity extraction. The definition of the relative error is as given in (21). Besides, the same surface is also solved by FEKO software with the RWG (linear and first-order) basis functions for different mesh lengths to obtain a reasonable comparison. As seen from Table 2, although FEKO is faster when comparing our formulations, the relative error results do not converge as desired, even using a fairly dense mesh in contrast to our study. As a result, the formulations used in FEKO do not achieve high accuracy, and the solution time is also longer when it uses dense mesh in order to improve accuracy.

Table 2. Comparison of periodic-MoM formulations for several mesh sizes.

This work					FEKO		
Mesh length	PGF error	Acceleration technique	Relative error	Solution time (s)	Mesh length	Relative error	Solution time (s)
$\lambda/10$	10^{-3}	Kummer	3.07×10^{-5}	249	$\lambda/10$	0.0223	0.355
					$\lambda/20$	0.0143	0.549
$\lambda/20$			6.63×10^{-7}	2442.9	$\lambda/30$	0.0115	1.148
					$\lambda/50$	0.0088	10.68
$\lambda/30$			4.40×10^{-7}	10832.9	$\lambda/100$	0.0063	242.9
					$\lambda/200$	0.0048	9465.7

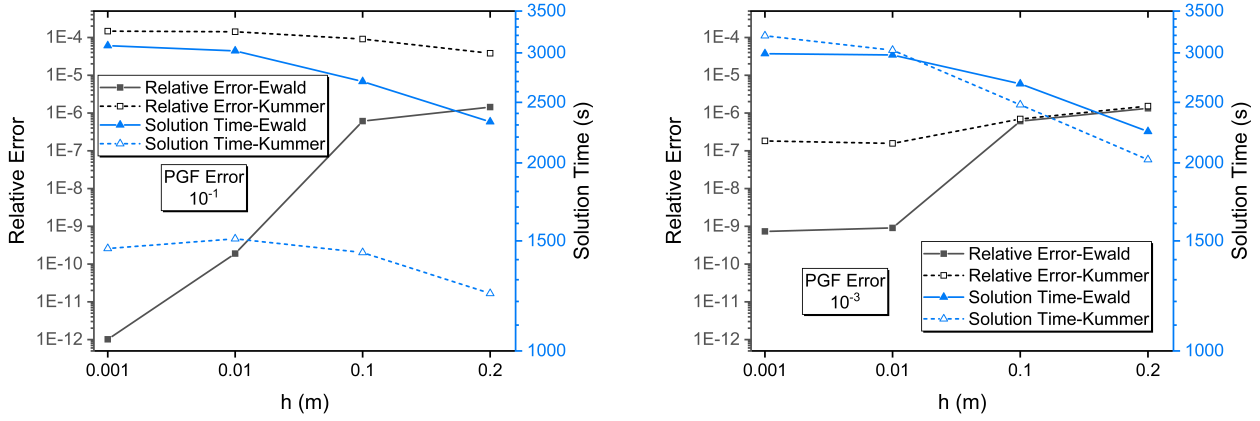
3.1.2. Effect of surface height

In order to compare the effects of acceleration techniques on the surface height, a 1-D sinusoidal surface is defined with a function $f(x) = -h\cos(2\pi x/L_x)$. Here, the lengths of unit cell are $L_x = L_y = 0.5$ m, and h parameter is changed with $h = 0.001$ m, $h = 0.01$ m, $h = 0.1$ m, and $h = 0.2$ m. The performance results of the Kummer's and Ewald's transformations with 10^{-1} and 10^{-3} convergence errors are given in Figures 3a, 3b, respectively. The incident angle of the plane wave is selected as $\theta^i = 30°$ and $\phi^i = 0°$, the polarization is horizontal, and the flat surface is discretized by triangles with an edge length of about 0.1λ. The solution frequency is selected as 300 MHz, and the minimum cutoff frequency (f_c) is found as 400 MHz from (22). As seen from Figure 3a, Kummer's transformation is always faster than Ewald's decomposition for high convergence error 10^{-1}, and, on the other hand, the accuracy for Ewald's transform is always better. However, when $|z - z'| \to 0$, Ewald's transform may converge faster than Kummer's for convergence errors less than 10^{-3}.

3.1.3. Effect of unit cell size

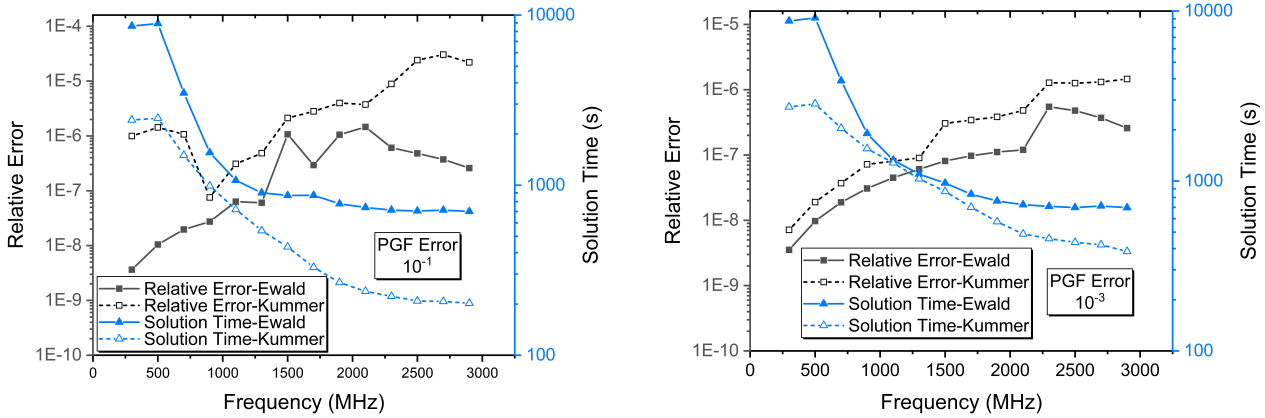
The size of a unit cell of a periodic surface can affect the performance of the acceleration techniques. For this analysis, a 1-D sinusoidal surface is utilized with a function $f(x) = -h\cos(2\pi x/L_x)$, where $h = 0.01$ m, $L_x = L_y = 0.0852$ m. The incident angle of the plane wave is chosen as $\theta^i = 10°$, $\phi^i = 0°$, and for the mesh average length is about 0.00852 m. Therefore, the minimum cutoff frequency is adjusted as 3000 MHz

for easier relative error comparison. The solution frequency is altered between 300 and 2900 MHz with 200 MHz intervals. This provides that the unit cell dimensions are electrically changing between about $0.0852\,\lambda$ and $0.8\,\lambda$. For 300–2900 MHz range, the relative errors and solution times are demonstrated in Figure 4. Herein, Kummer's and Ewald's transformations with 10^{-1} and 10^{-3} convergence errors are compared in Figures 4a and 4b, respectively. For high convergence errors, Kummer's transformation is always faster than Ewald's one with similar accuracy values. Besides, as seen from previous and present results, lower convergence errors are not really necessary to achieve the desired accuracy. When comparing solution times, Kummer's transform with 10^{-1} convergence error is always shorter. However, for larger unit cell dimensions, Ewald's transform can be faster for lower convergence errors than 10^{-3}.



PGF error 10^{-1} PGF error 10^{-3}

Figure 3. Relative error and solution time results for a sinusoidal surface with various h values at 300 MHz.



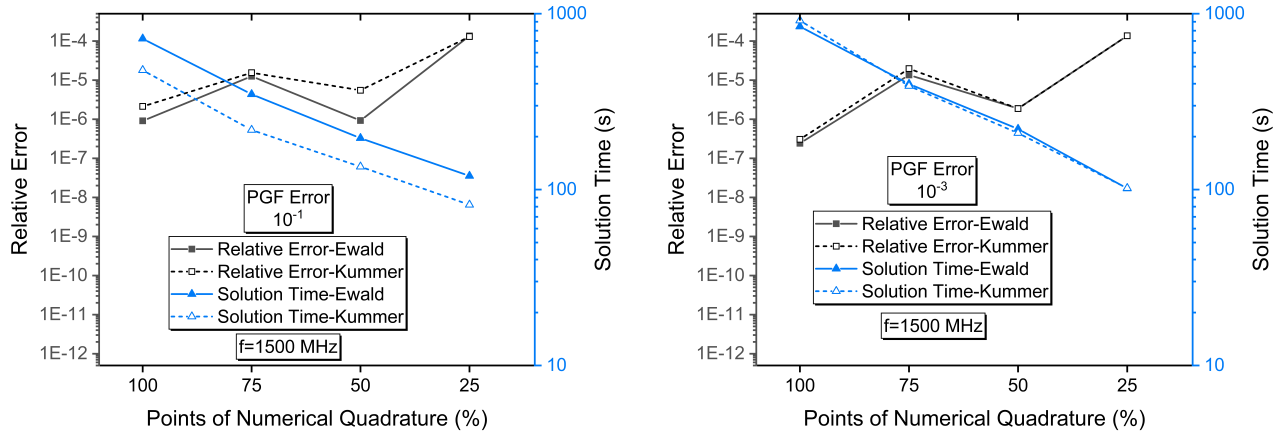
PGF error 10^{-1} PGF error 10^{-3}

Figure 4. Relative error and solution time results of a sinusoidal surface with $L_x = L_y = 0.0852$ m and $h = 0.01$ m for various operating frequencies.

3.1.4. Effect of numerical integration

The quality of numerical integration is also vitally important. In order to achieve high accuracy, the points used in numerical quadrature were initially used in high numbers. In addition, the number of these points

changes dynamically according to the distance between the observation and source triangle facets. Hence, the total number of points in numerical integration in this study changes between 36, 169, 361, 729, and 3318 for near and far triangles facets. These values are considered a reference to assure high accuracy. In Figure 5, these point numbers are reduced as a percentage, and the results are analyzed in terms of accuracy and solution time. The surface function is selected again $f(x) = -h\cos(2\pi x/L_x)$, where $h = 0.01$ m, $L_x = L_y = 0.0852$ m. The solution frequency is selected as 1500 MHz, the incident angle of the plane wave is $\theta^i = 10°$, $\phi^i = 0°$, and for the mesh size, the length of one side of the triangles is about 0.00852 m. Kummer's and Ewald's transformations with 10^{-1} and 10^{-3} convergence errors are also depicted in Figures 5a and 5b, respectively. As seen from this figure, the solution time can be increased excessively by decreasing the quality of numerical integration if one desires high accuracy. However, if high accuracy is really entailed, adjusting PGF convergence error, reducing points of numerical quadrature, and determining an intelligent choice of the acceleration technique for some instances make the speed of the numerical code faster while maintaining considerable accuracy.



PGF error 10^{-1} PGF error 10^{-3}

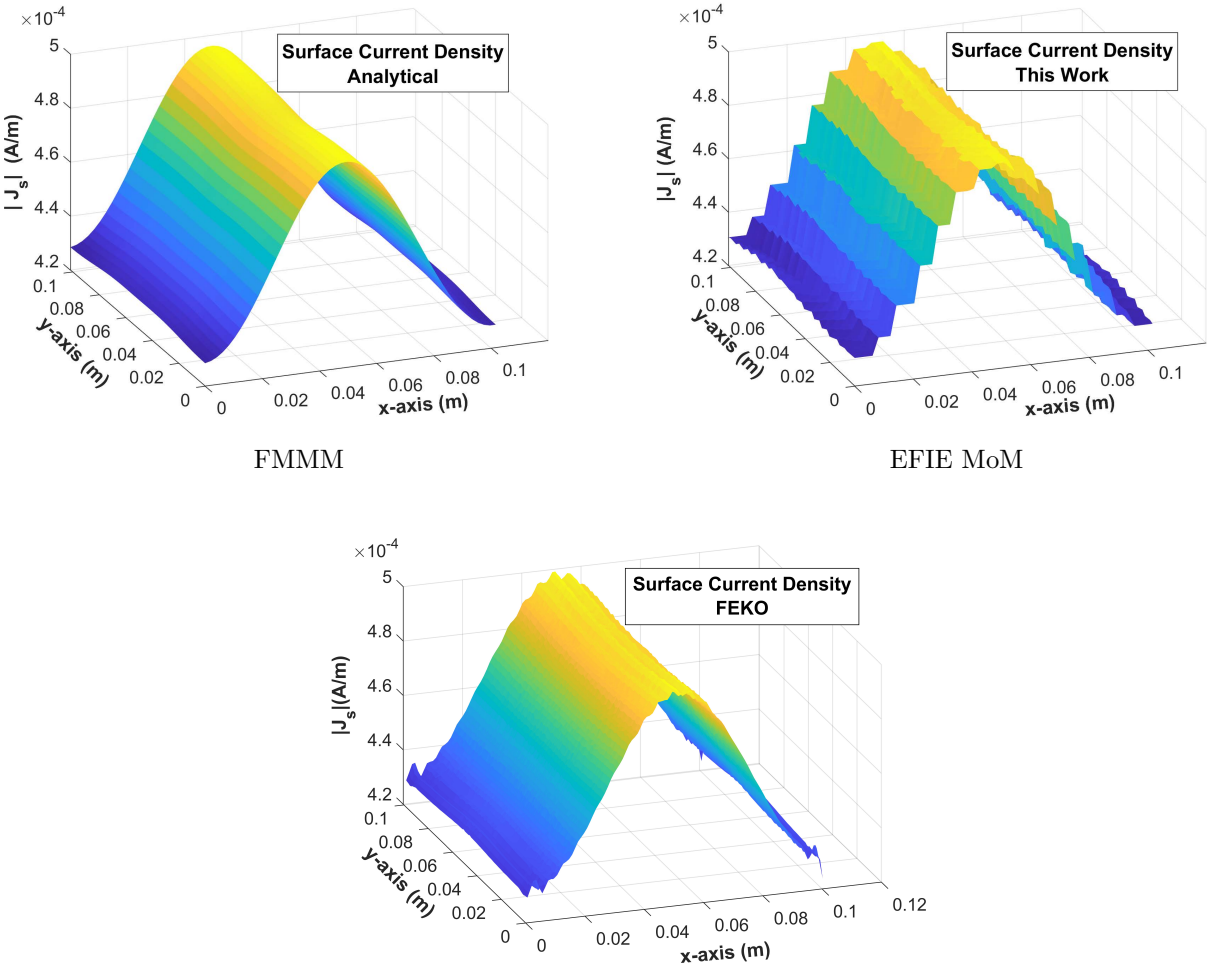
Figure 5. Relative error and solution time results for a sinusoidal surface with various numerical quadrature points as percentages.

3.2. Comparison of periodic-MoM solution with analytical results for various rough surfaces

In this subsection, the accuracy test of the periodic-MoM solution is conducted for various periodic rough surface problems. To perform this validation, the rough surface height is chosen to be small compared to the wavelength. In this way, the solution region where Rayleigh's assumption is valid is preserved, and the analytical and semianalytical equations can be obtained as seen in Appendices 1 and 2.

3.2.1. Comparative results for a 2-D sinusoidal surface

The periodic rough surface is assumed as a simple well-known sinusoidal that avoids the complexity of the IE method's validation with the Rayleigh-based methods. Selecting sinusoidal functions as a surface model facilitates calculating Rayleigh-based methods' coefficients analytically (see Appendices 1 and 2). Thus, the surface function is considered $z = f(x,y) = -h\left[\cos(2\pi x/L_x) + \cos(2\pi y/L_y)\right]$, where $h = 0.0016$ m, $L_x = L_y = 0.1016$ m. The incident wave is horizontal polarization and is about at a low-grazing angle of 85°. As seen in Figure 6, the surface current densities are evaluated with the FMMM, the periodic-MoM, and FEKO, respectively. The numerical surface current in this work agrees well with the analytic one.



FMMM EFIE MoM

FEKO

Figure 6. Induced surface current densities on one period of infinite, conductive sinusoidal surface at 1.5 GHz.

The total scattered fields are also calculated for several frequencies in Figure 7, where the observation point is at $x = y = 0$ m, and $z = 100$ m. In this figure, the EFIE-MoM solution's validation is ensured in a proper frequency region for the SPM and FMMM. The derivation of the FMMM is given to calculate the unknown coefficients of (23) using numerical integration for any surface function in Appendix 1. An analytical formulation is also derived for this sinusoidal surface with Bessel identity in Appendix 2. The arbitrary-order SPM solution is acquired by an iterative solution [4]. Consequently, FMMM offers a more straightforward formulation than higher-order SPM, and the solution time is slower in the SPM. These two Rayleigh-based methods are also compared within themselves for this surface (see Figure 7). Furthermore, for several observation points at x- and z-directions, the scattered fields are also compared with the analytical solution given in Appendix 2. The magnitudes of scattered E-fields are compared for observation points at z-direction by starting from the locations where they are very close to the surface in Figure 8a. The scattered E-fields are also evaluated for x-direction in Figure 8b. Here, FEKO results are also given in the figures for comparison. In Figure 7, the averaged edge lengths of triangles in the meshed structure are about 0.01 m in the EFIE-MoM solution and

0.0025 m in the FEKO simulation to obtain the expected accuracy. On the other hand, for the solutions of several observation points at 1500 MHz, the mesh structure used in the EFIE-MoM and FEKO solutions is the same as that depicted in Figure 8b, where the averaged triangle edge length corresponds to about $\lambda/20$. As a result, as seen from the figures, all the numerical results of the EFIE-MoM formulation are very satisfactory.

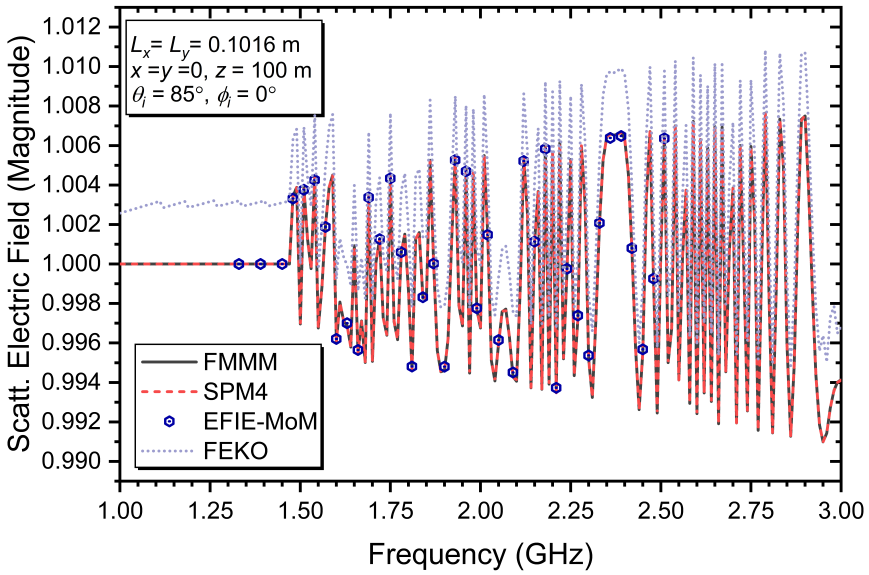
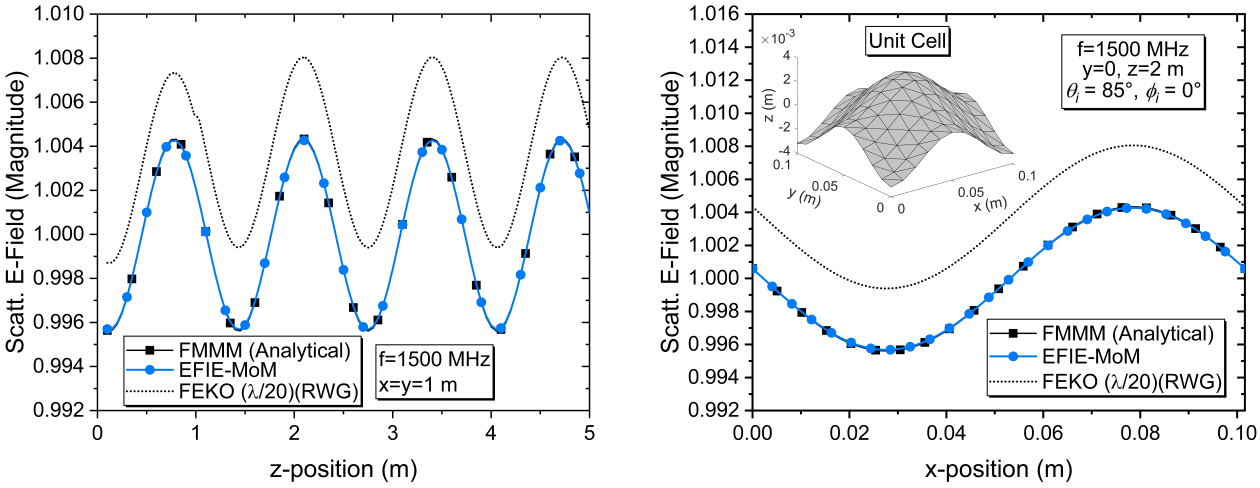


Figure 7. Magnitude of total scattered E-field from infinite, conducting sinusoidal surface as a function of frequency for TE polarization.



Along z-axis

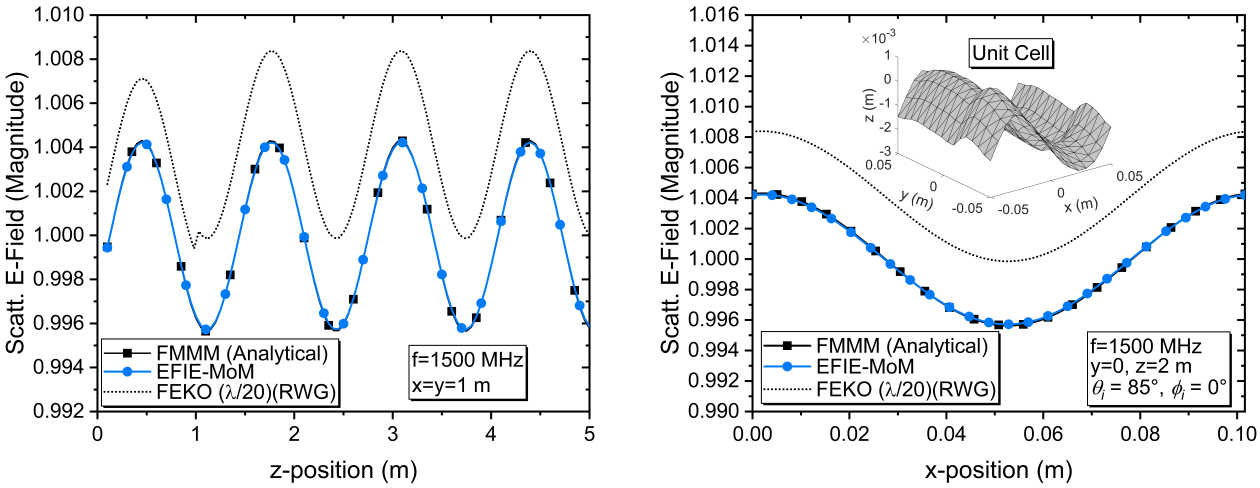
Along x-axis in unit cell

Figure 8. Total scattered E-field with respect to several observation points for a sinusoidal surface.

3.2.2. Comparative results for an arbitrarily rough periodic surface

A random surface is also generated by a Gaussian correlation function with an RMS height of $h = 0.0032$ m and a correlation length of $l = 0.09$ m to compare the semianalytical formulation in Appendix 1 with the periodic-MoM solution. The lengths of unit cell are $L_x = L_y = 0.1016$ m, and computed scattering E-fields are shown

in Figure 9. Here, the incident wave is horizontally polarized and at a low grazing angle of approximately 85°. The results agree well with EFIE-MoM solutions. A numerical quadrature with 25 points is used in calculating integrals of in (37)–(42), and the total solution time of the FMMM takes 8.6 s. The numerical derivative is also employed in this semianalytical solution. Compared to the EFIE-MoM solution in terms of solution time, the full-wave solution takes about 8523 s. The results are shown that the full-wave periodic-MoM solution provides enough accuracy. In contrast, the solution time of this full-wave method can be reduced, as well as the semianalytical solution can be employed for any rough surface having a small height and slope. Besides, the results from FEKO are also given in Figure 9 for a mesh size with an average triangle edge length of $\lambda/20$, where the RWG basis function is also employed in obtaining numerical results. The unit cell with its mesh structure utilized in the EFIE-MoM and FEKO solutions is depicted in Figure 9b.



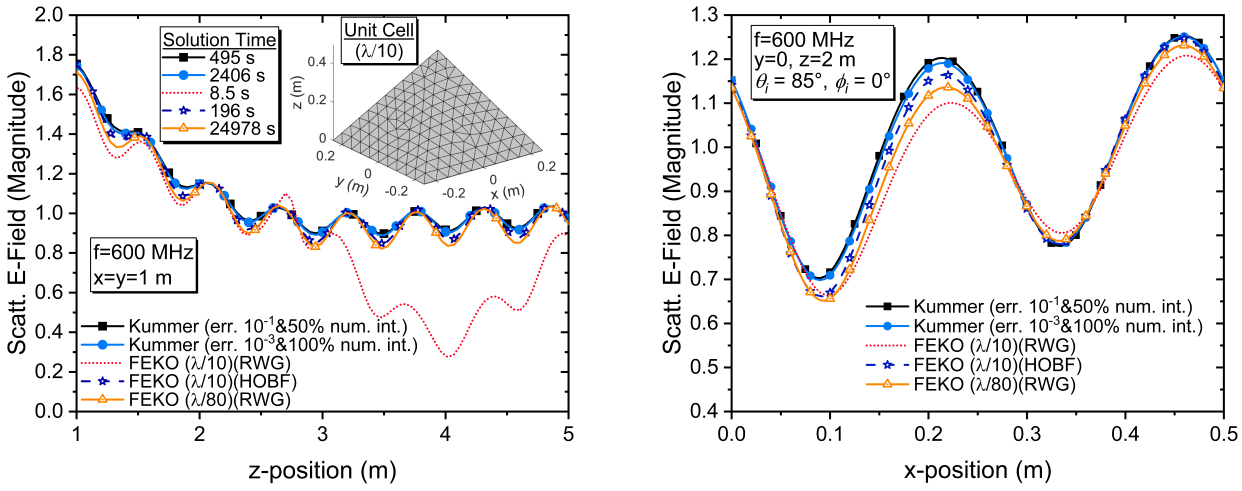
Along z-axis Along x-axis in unit cell

Figure 9. Total scattered E-field with respect to several observation points for a random surface.

3.3. Comparison of our periodic-MoM solution with FEKO results for highly rough surfaces

In this subsection, the degree of roughness of the periodic surface is increased to a level where the Rayleigh hypothesis is not valid. As shown in Figure 10, a pyramidal surface $L_x = L_y = 0.499$ m is chosen in this context. Here, this rough surface is singular, and its height is 0.499 m. The observation points and the incident angle of the plane wave are similar to the previous simulations, and the solution frequency is 600 MHz. Figures 10a and 10b show the total scattered E-fields in the z-direction and the x-direction, respectively. In the first EFIE-MoM solution, the number of points used in the numerical integration is reduced by 50%, and Kummer's transform is employed with a convergence error of 10^{-1}. Secondly, the convergence error is reduced to 10^{-3} without decreasing numerical integration points. In addition, to compare the EFIE-MoM results, FEKO software is used with several mesh types and sizes. The first comparison is performed using the RWG basis functions with the same mesh structure as the EFIE-MoM solution. Then, a higher-order basis function (HOBF) with the same mesh size and a very dense mesh ($\lambda/80$) with the RWG basis functions are employed respectively to provide higher accuracy. The unit cell, the mesh structure, and the elapsed times for the computations are also demonstrated in Figure 10a. It should be noted that for the same mesh type and size, the accuracy of the present work for this example is better than the FEKO simulation results, as can be

seen from Figure 10 (the red-colored dotted line). On the other hand, as discussed in detail in Section 3.1, the solution time is considerably shorter for Kummer's transform with a 10^{-1} high error level.



Along z-axis

Along x-axis in unit cell

Figure 10. Total scattered E-field with respect to several observation points for a pyramidal rough surface.

4. Conclusion

In this paper, a numerical method based on a 3-D MoM solution that addressed scattering problems from arbitrarily rough, periodic 2-D conductive surfaces that simulate sea or ground surfaces under plane wave illumination has been developed. The special basis and testing functions have been employed for handling edge discontinuities in the unit cell boundaries. The importance and necessities of used methods in the periodic-MoM formulations have been precisely discussed, part by part. The convergence speed of Kummer's and Ewald's transformations for several scattering scenarios was discussed in detail. Furthermore, the singularities in these methods were examined, and no significant difference was observed in terms of solution time and accuracy. The extraction of near- and far-field equations was also derived in this study. Besides, this study answers whether acceleration techniques with low and high convergence errors are necessary to obtain the desired accuracy and solution time in running the numerical code for various scattering problems. According to the obtained results, Kummer's transform with 10^{-1} convergence error improves the solution speed without changing the accuracy significantly. The combinations of the acceleration techniques with the height of the surface, mesh size, unit cell dimensions, frequency, and quality of the numerical integration are also vital for achieving the desired performance in numerical codes. Consequently, the acceleration techniques can be selected according to the size and height of the periodic surface. Also, the developed MoM code is more successful than commercial software that uses the same periodic-MoM approach in terms of accuracy, and on the other hand, the solution time can be shorter utilizing a faster programming language. Moreover, a semianalytical solution called FMMM has been proposed for 2-D periodic arbitrary rough surfaces for the first time in this paper to validate periodic-MoM formulations as an alternative to the SPM solution. This analytical approach is already employed for 1-D sinusoidal surfaces in the literature. However, the present study has extended it to any arbitrary 2-D rough periodic surfaces. The FMMM solution is more straightforward than the SPM while it gives fully consistent results with the SPM and our periodic-MoM formulations.

Acknowledgment

This work was supported by the Scientific and Technological Research Council of Turkey (TÜBİTAK) under Project Number 119N196.

References

[1] Rice SO. Reflection of electromagnetic waves from slightly rough surfaces. Communications on Pure and Applied Mathematics 1951; 4 (2–3): 351-378. doi:10.1002/cpa.3160040206.

[2] Millar RF. On the Rayleigh assumption in scattering by a periodic surface. II. Mathematical Proceedings of the Cambridge Philosophical Society 1971; 69 (1): 217-225. doi:10.1017/S0305004100046570

[3] Johnson JT. Third-order small-perturbation method for scattering from dielectric rough surfaces.Journal of the Optical Society of America A 1999; 16 (11): 2720-2736. doi:10.1364/josaa.16.002720

[4] Demir MA, Johnson JT. Fourth and higher order small perturbation solution for scattering from dielectric rough surfaces. Journal of the Optical Society of America A 2003; 20 (12): 2330-2337. doi:10.1364/JOSAA.20.002330

[5] Guo LX, Liang Y, Li J, Wu ZS. A high order integral SPM for the conducting rough surface scattering with the tapered wave incidence-TE case. Progress in Electromagnetics Research 2011; 114 :333-352. doi:10.2528/PIER11011605

[6] Ishimaru A. Periodic Structures and Coupled-Mode Theory. In: Electromagnetic Wave Propagation, Radiation, and Scattering. Piscataway, NJ 08854, USA: Wiley-IEEE Press, 2017, pp. 201-231. doi:10.1002/9781119079699.ch7

[7] Norman A, Nyquist DP, Rothwell E, Chen KM, Ross J et al. Transient scattering of a short pulse from a conducting sinusoidal surface. Journal of Electromagnetic Waves and Applications 1996; 10 (4): 461-487. doi:10.1163/156939396X01062

[8] Thorsos EI. The validity of the Kirchhoff approximation for rough surface scattering using a Gaussian roughness spectrum. Journal of the Acoustical Society of America 1988; 83 (1): 78-92. doi:10.1121/1.396188

[9] West JC. On the Control of Edge Diffraction in Numerical Rough Surface Scattering Using Resistive Tapering. IEEE Transactions on Antennas and Propagation 2003; 51 (11): 3180-3183. doi:10.1109/TAP.2003.818775

[10] Spiga P, Soriano G, Saillard M. Scattering of electromagnetic waves from rough surfaces: A boundary integral method for low-grazing angles. IEEE Transactions on Antennas and Propagation 2008; 56 (7): 2043-2050. doi:10.1109/TAP.2008.924710

[11] Chen R, West JC. Analysis of Scattering from Rough Surfaces at Large Incidence Angles Using a Periodic-Surface Moment Method. IEEE Transactions on Geoscience and Remote Sensing 1995; 33 (5): 1206-1213. doi:10.1109/36.469484

[12] DeSanto J, Erdmann G, Hereman W, Krause B, Misra M et al. Theoretical and computational aspects of scattering from periodic surfaces: Two-dimensional perfectly reflecting surfaces using the spectral-coordinate method. Waves Random Media 2001; 11 (4):455-487. doi:10.1088/0959-7174/11/4/306

[13] Barzegar-Parizi S, Shishegar AA. Electromagnetic wave scattering analysis from 2-D periodic rough surfaces using complex images technique. IEEE Transactions on Geoscience and Remote Sensing 2015; 53 (2):862-868. doi:10.1109/TGRS.2014.2329995

[14] Yildiz S, Altuncu Y, Ozdemir O. Scattering of Electromagnetic Waves by Periodic Rough Surfaces. IEEE Transactions on Geoscience and Remote Sensing 2008; 46 (9):2599-2606.

[15] Wang D, Yung EKN, Chen RS, Ding DZ, Tang WC. On evaluation of the green function for periodic structures in layered media. IEEE Antennas and Wireless Propagation Letters 2004; 3 (1): 133-136. doi:10.1109/LAWP.2004.831076

[16] Capolino F, Wilton DR, Johnson WA. Efficient computation of the 2-D Green's function for 1-D periodic structures using the Ewald method. IEEE Transactions on Antennas and Propagation 2005; 53 (9): 2977-2984. doi:10.1109/TAP.2005.854556

[17] Park MJ, Lee B. Efficient calculation of the Green's function for 2-D periodic line sources using Ewald method. IEEE Antennas and Wireless Propagation Letters 2009; 8 (4): 565-567. doi:10.1109/LAWP.2009.2022652

[18] Lampe R, Klock P, Mayes P. Integral Transforms Useful for the Accelerated Summation of Periodic, Free-Space Green's Functions. IEEE Transactions on Microwave Theory and Techniques 1985; 33 (8): 734-736. doi:10.1109/TMTT.1985.1133067

[19] Singh S, Richards WF, Zinecker JR, Wilton DR. Communications: Accelerating the Convergence of Series Representing the Free Space Periodic Green's Function. IEEE Transactions on Antennas and Propagation 1990; 38 (12): 1958-1962. doi:10.1109/8.60985

[20] Valerio G, Baccarelli P, Burghignoli P, Galli A. Comparative analysis of acceleration techniques for 2-D and 3-D Green's functions in periodic structures along one and two directions. IEEE Transactions on Antennas and Propagation 2007; 55 (6): 1630-1643.doi:10.1109/TAP.2007.897340

[21] Jordan KE, Richter GR, Sheng P. An efficient numerical evaluation of the Green's function for the Helmholtz operator on periodic structures. Journal of Computational Physics 1986; 63 (1): 222-235. doi:10.1016/0021-9991(86)90093-8

[22] Stevanović I, Crespo-Valero P, Blagović K, Bongard F, Mosig JR. Integral-equation analysis of 3-D metallic objects arranged in 2-D lattices using the ewald transformation. IEEE Transactions on Microwave Theory and Techniques 2006; 54 (10): 3688-3697. doi:10.1109/TMTT.2006.882876

[23] Simon PS. Modified RWG basis functions for analysis of periodic structures. IEEE MTT-S International Microwave Symposium Digest; Seattle, WA, USA; 2002.pp. 2029-2032. doi:10.1109/MWSYM.2002.1012266

[24] Hu FG, Song J. Integral-equation analysis of scattering from doubly periodic array of 3-D conducting objects. IEEE Transactions on Antennas and Propagation 2011; 59 (12): 4569-4578. doi:10.1109/TAP.2011.2165466

[25] Millar RF. The Rayleigh hypothesis and a related least-squares solution to scattering problems for periodic surfaces and other scatterers. Radio Science 1973; 8 (8-9): 785-796. doi:10.1029/RS008i008p00785

[26] Wilton DR, Rao SSM, Glisson AW. Electromagnetic Scattering By Surfaces of Arbitrary Shape. IEEE Transactions on Antennas and Propagation 1982; 30 (3): 409-418. doi:10.1109/TAP.1982.1142818

[27] Dunavant DA. High Degree Efficient Symmetrical Gaussian Quadrature Rules for the Triangle. International Journal for Numerical Methods in Engineering 1985; 21: 1129–1148. doi:10.1002/nme.1620210612

[28] Graglia RD. On the Numerical Integration of the Linear Shape Functions Times the 3-D Green's Function or its Gradient on a Plane Triangle. IEEE Transactions on Antennas and Propagation 1993; 41 (10): 1448-1455. doi:10.1109/8.247786

[29] Duffy MG. Quadrature Over a Pyramid or Cube of Integrands with a Singularity at a Vertex. SIAM Journal on Numerical Analysis 1982; 19 (6): 1260-1262. doi:10.1137/0719090

[30] Wilton DR, Wilton DR, Rao SM, Glisson AW et al. Potential Integrals for Uniform and Linear Source Distributions on Polygonal and Polyhedral Domains. IEEE Transactions on Antennas and Propagation 1984; 32 (3): 276-281. doi:10.1109/TAP.1984.1143304

[31] Eibert TF, Hansen V. On the Calculation of Potential Integrals for Linear Source Distributions on Triangular Domains. IEEE Transactions on Antennas and Propagation 1995; 43 (12): 1499-1502. doi:10.1109/8.475946

[32] Stevanoviæ I, Mosig JR. Periodic Green's Function for Skewed 3-D Lattices Using the Ewald Transformation. Microwave and Optical Technology Letters 2007; 49 (6): 1353-1357. doi:10.1002/mop.22429

[33] Khayat MA, Wilton DR. Numerical Evaluation of Singular and Near-Singular Potential Integrals. IEEE Transactions on Antennas and Propagation 2005; 53 (10): 3180-3190. doi:10.1109/TAP.2005.856342

[34] Adanir S, Alatan L. Singularity Cancellation for Accurate MoM Analysis of Periodic Planar Structures in Layered Media. IEEE Antennas Wirel Propag Lett. 2020; 19 (8): 1301-1305. doi:10.1109/LAWP.2020.2997798

[35] Van Tonder J, Jakobus U. Infinite periodic boundary conditions in FEKO. Applied Computational Electromagnetic Society Journal. 2009; 24:584–591.

Appendices

Appendix 1. Arbitrary surface solution of FMMM

After invoking Rayleigh hypothesis, a general representation of the scattered field can be expressed with vertical and horizontal fields

$$\overline{E}^{s}(\overline{r}) = \sum_{m=-\infty}^{\infty}\sum_{n=-\infty}^{\infty}\left(\hat{h}_{mn}A_{mn} + \hat{v}_{mn}B_{mn}\right)e^{-j\overline{k}_s\cdot\overline{r}} \tag{23}$$

where $\hat{h}_{mn}$ and $\hat{v}_{mn}$ is the horizontal and vertical unit vectors for each Floquet mode. The magnetic field intensity and the current density on the surface

$$\overline{H}^{s}(\overline{r}) = \frac{\hat{k}_s\times\overline{E}^{s}(\overline{r})}{\eta_0} \quad \text{and} \quad \overline{J}^{s}(\overline{r}) = \hat{n}\times\left[\overline{H}^{i}(\overline{r}) + \overline{H}^{s}(\overline{r})\right] \tag{24}$$

Definitions of the units vectors are as follows:

$$\hat{h}_i = \frac{\overline{k}_i\times\hat{z}}{\left\|\overline{k}_i\times\hat{z}\right\|}, \quad \hat{v}_i = \hat{h}_i\times\hat{k}_i, \quad \hat{h}_{mn} = \frac{\overline{k}_s\times\hat{z}}{\left\|\overline{k}_s\times\hat{z}\right\|}, \quad \hat{v}_{mn} = \hat{h}_{mn}\times\hat{k}_s \tag{25}$$

Here,

$$\hat{h}_{mn} = \frac{1}{\beta_{mn}}\left(\hat{x}\beta_n - \hat{y}\beta_m\right), \quad \hat{v}_{mn} = -\hat{x}\frac{\beta_m q_{mn}}{\beta_{mn}\beta_0} - \hat{y}\frac{\beta_n q_{mn}}{\beta_{mn}\beta_0} + \hat{z}\frac{\beta_{mn}}{\beta_0} \tag{26}$$

and the unit normal vector of the surface:

$$\hat{n} = \frac{\nabla\left[z - f(x,y)\right]}{\left\|\nabla\left[z - f(x,y)\right]\right\|} = \frac{\hat{z} - \hat{x}\frac{\partial f(x,y)}{\partial x} - \hat{y}\frac{\partial f(x,y)}{\partial y}}{\sqrt{1 + \frac{\partial^2 f(x,y)}{\partial x^2} + \frac{\partial^2 f(x,y)}{\partial y^2}}} = \frac{\hat{z} - \hat{x}f_x - \hat{y}f_y}{\sqrt{1 + f_x^2 + f_y^2}} \tag{27}$$

By subjecting boundary conditions to (1) and (23) on the surface

$$\left[\left(\hat{z} - \hat{x}f_x - \hat{y}f_y\right)\times\left(\overline{E}^{i} + \overline{E}^{s}\right)\right]\Big|_{z=f(x,y)} = 0 \tag{28}$$

$$\left[\left(\hat{z} - \nabla_t f\right)\times\left(\hat{e}_i E_0 e^{-j\overline{k}_i\cdot\overline{r}}\right) = -\left(\hat{z} - \nabla_t f\right)\times\sum_{m,n=-\infty}^{\infty}\left(\hat{h}_{mn}A_{mn} + \hat{v}_{mn}B_{mn}\right)e^{-j\overline{k}_s\cdot\overline{r}}\right]\Big|_{z=f(x,y)} \tag{29}$$

By the simplifications

$$\left(\hat{z} - \nabla_t f\right)\times\left(\hat{e}_i E_0 e^{jqf}\right) = -\left(\hat{z} - \nabla_t f\right)\times\sum_{m,n=-\infty}^{\infty}\left(\hat{h}_{mn}A_{mn} + \hat{v}_{mn}B_{mn}\right)e^{-jq_{mn}f}e^{j2\pi(mx/L_x + ny/L_y)} \tag{30}$$

where $f = f(x,y)$ and $\hat{e}_i E_0 = E_x\hat{x} + E_y\hat{y} + E_z\hat{z}$. Derivation of the vector products:

$$\left(\hat{z} - \nabla_t f\right)\times\hat{e}_i E_0 = -\hat{x}\left(f_y E_z + E_y\right) + \hat{y}\left(E_x + f_x E_z\right) + \hat{z}\left(f_y E_x - f_x E_y\right) \tag{31}$$

$$\left(\hat{z} - \nabla_t f\right)\times\hat{h}_{mn} = \hat{x}\frac{\beta_m}{\beta_{mn}} + \hat{y}\frac{\beta_n}{\beta_{mn}} + \hat{z}\left(f_x\frac{\beta_m}{\beta_{mn}} + f_y\frac{\beta_n}{\beta_{mn}}\right) \tag{32}$$

$$(\hat{z}-\nabla_t f)\times\hat{v}_{mn}=-\hat{x}\left(f_y\frac{\beta_{mn}}{\beta_0}-\frac{\beta_n q_{mn}}{\beta_{mn}\beta_0}\right)-\hat{y}\left(\frac{\beta_m q_{mn}}{\beta_{mn}\beta_0}-f_x\frac{\beta_{mn}}{\beta_0}\right)+\hat{z}\left(f_x\frac{\beta_n q_{mn}}{\beta_{mn}\beta_0}-f_y\frac{\beta_m q_{mn}}{\beta_{mn}\beta_0}\right) \tag{33}$$

Using the finding above linear equation system can be obtained by the Galerkin method for x and y unit vector components, so the x-component of the equation system can be derived as

$$\left[A_{mn}\frac{\beta_m}{\beta_{mn}}+B_{mn}\left(\frac{\beta_n q_{mn}}{\beta_{mn}\beta_0}-f_y\frac{\beta_{mn}}{\beta_0}\right)\right]e^{-jq_{mn}f}e^{j2\pi[(u-m)x/L_x+(v-n)y/L_y]}=\left(f_yE_z+E_y\right)e^{jqf}e^{j2\pi[ux/L_x+vy/L_y]} \tag{34}$$

and y-component of the system

$$\begin{aligned}\left[A_{mn}\frac{\beta_n}{\beta_{mn}}+B_{mn}\left(f_x\frac{\beta_{mn}}{\beta_0}-\frac{\beta_m q_{mn}}{\beta_{mn}\beta_0}\right)\right]e^{-jq_{mn}f}e^{j2\pi[(u-m)x/L_x+(v-n)y/L_y]}&\\ =-\left(f_xE_z+E_x\right)e^{jqf}e^{j2\pi[ux/L_x+vy/L_y]}&\end{aligned} \tag{35}$$

can also be obtained. As a result, the solution of (34) and (35) is in the form of:

$$KX=L \tag{36}$$

Here, $K\in\mathbb{C}^{u\times v\times m\times n\times 2\times 2}$, $X\in\mathbb{C}^{m\times n\times 2\times 1}$, and $L\in\mathbb{C}^{u\times v\times 2\times 1}$ are tensors, and they can be turned into a matrix form. Thus, $\overline{\overline{K}}$ matrices can be given as

$$\overline{\overline{K}}_{11}=\frac{1}{L_xL_y}\int_0^{L_x}\int_0^{L_y}\frac{\beta_m}{\beta_{mn}}e^{-jq_{mn}f}e^{j2\pi[(u-m)x/L_x+(v-n)y/L_y]}dxdy \tag{37}$$

$$\overline{\overline{K}}_{12}=\frac{1}{L_xL_y}\int_0^{L_x}\int_0^{L_y}\left(\frac{\beta_n q_{mn}}{\beta_{mn}\beta_0}-f_y\frac{\beta_{mn}}{\beta_0}\right)e^{-jq_{mn}f}e^{j2\pi[(u-m)x/L_x+(v-n)y/L_y]}dxdy \tag{38}$$

$$\overline{\overline{K}}_{21}=\frac{1}{L_xL_y}\int_0^{L_x}\int_0^{L_y}\frac{\beta_n}{\beta_{mn}}e^{-jq_{mn}f}e^{j2\pi[(u-m)x/L_x+(v-n)y/L_y]}dxdy \tag{39}$$

$$\overline{\overline{K}}_{22}=\frac{1}{L_xL_y}\int_0^{L_x}\int_0^{L_y}\left(f_x\frac{\beta_{mn}}{\beta_0}-\frac{\beta_m q_{mn}}{\beta_{mn}\beta_0}\right)e^{-jq_{mn}f}e^{j2\pi[(u-m)x/L_x+(v-n)y/L_y]}dxdy \tag{40}$$

and $\overline{\overline{L}}$ matrices

$$\overline{\overline{L}}_{11}=\frac{1}{L_xL_y}\int_0^{L_x}\int_0^{L_y}\left(f_yE_z+E_y\right)e^{jqf}e^{j2\pi[ux/L_x+vy/L_y]}dxdy \tag{41}$$

$$\overline{\overline{L}}_{21}=-\frac{1}{L_xL_y}\int_0^{L_x}\int_0^{L_y}\left(f_xE_z+E_x\right)e^{jqf}e^{j2\pi[ux/L_x+vy/L_y]}dxdy \tag{42}$$

are obtained. Consequently, after finding the solution of each integral numerically, these matrices are written in the form below. A_{mn} and B_{mn} unknowns are found after solving this linear equation system:

$$\begin{bmatrix}\overline{\overline{K}}_{11} & \overline{\overline{K}}_{12}\\ \overline{\overline{K}}_{21} & \overline{\overline{K}}_{22}\end{bmatrix}\begin{bmatrix}\overline{\overline{A}}_{mn}\\ \overline{\overline{B}}_{mn}\end{bmatrix}=\begin{bmatrix}\overline{\overline{L}}_{11}\\ \overline{\overline{L}}_{21}\end{bmatrix} \tag{43}$$

Appendix 2. Sinusoidal surface solution of FMMM

If the rough surface is chosen as a simple sinusoidal function as $z = f(x,y) = -h\left[\cos\left(2\pi x/L_x\right) + \cos\left(2\pi y/L_y\right)\right]$, the FMMM solution can be obtained by Bessel functions for such a type of sinusoidal surface function, so $\overline{\overline{K}}$ matrices above can form as follows

$$\overline{\overline{K}}_{11} = \frac{\beta_m}{\beta_{mn}} (j)^{|u-m|} (j)^{|v-n|} J_{|u-m|}(q_{mn}h) J_{|v-n|}(q_{mn}h) \tag{44}$$

$$\begin{aligned}\overline{\overline{K}}_{12} = &-\frac{\beta_{mn}}{\beta_0}\frac{h\pi}{L_y}(j)^{|u-m|} J_{|u-m|}(q_{mn}h)\left[(j)^{|v-n|} J_{|v-n+1|}(q_{mn}h) + (j)^{|v-n|} J_{|v-n-1|}(q_{mn}h)\right] \\ &+ \frac{\beta_n q_{mn}}{\beta_{mn}\beta_0}(j)^{|u-m|}(j)^{|v-n|} J_{|u-m|}(q_{mn}h) J_{|v-n|}(q_{mn}h)\end{aligned} \tag{45}$$

$$\overline{\overline{K}}_{21} = \frac{\beta_n}{\beta_{mn}} (j)^{|u-m|} (j)^{|v-n|} J_{|u-m|}(q_{mn}h) J_{|v-n|}(q_{mn}h) \tag{46}$$

$$\begin{aligned}\overline{\overline{K}}_{22} = &\frac{\beta_{mn}}{\beta_0}\frac{h\pi}{L_X}(j)^{|v-n|} J_{|v-n|}(q_{mn}h)\left[(j)^{|u-m|} J_{|u-m+1|}(q_{mn}h) + (j)^{|u-m|} J_{|u-m-1|}(q_{mn}h)\right] \\ &- \frac{\beta_m q_{mn}}{\beta_{mn}\beta_0}(j)^{|u-m|}(j)^{|v-n|} J_{|u-m|}(q_{mn}h) J_{|v-n|}(q_{mn}h)\end{aligned} \tag{47}$$

and $\overline{\overline{L}}$ matrices

$$\overline{\overline{L}}_{11} = -\frac{E_z h}{L_y}(-j)^{|u|} J_{|u|}(qh)\left[(-j)^{|v|} J_{|v+1|}(qh) + (-j)^{|v|} J_{|v-1|}(qh)\right] + E_y (-j)^{|u|+|v|} J_{|u|}(qh) J_{|v|}(qh) \tag{48}$$

$$\overline{\overline{L}}_{21} = \frac{E_z h}{L_x}(-j)^{|v|} J_{|v|}(qh)\left[(-j)^{|u|} J_{|u+1|}(qh) + (-j)^{|u|} J_{|u-1|}(qh)\right] - E_x (-j)^{|u|+|v|} J_{|u|}(qh) J_{|v|}(qh) \tag{49}$$

Thus, these matrices are written in the form in Equation (43), and the solution is obtained.

Appendix 3. General near-field equation of MoM for observation points just above the surface

The double gradient of (6):

$$\nabla\nabla G_p(\overline{r}|\overline{r}') = -G_p(\overline{r}|\overline{r}')\begin{bmatrix} \beta_m^2 & \beta_m\beta_n & \beta_m q_{mn}\frac{(z-z')}{|z-z'|} \\ \beta_n\beta_m & \beta_n^2 & \beta_n q_{mn}\frac{(z-z')}{|z-z'|} \\ q_{mn}\beta_m\frac{(z-z')}{|z-z'|} & q_{mn}\beta_n\frac{(z-z')}{|z-z'|} & q_{mn}^2\left[\frac{|z-z'|^2-(z-z')^2}{(-jq_{mn})|z-z'|(z-z')^2} + \frac{(z-z')^2}{|z-z'|^2}\right] \end{bmatrix} \tag{50}$$